Efficient and Stable Tin Perovskite Solar Cells Enabled by Graded Heterostructure of Light-Absorbing Layer

Tianhao Wu, Danyu Cui, Xiao Liu, Xiangyue Meng, Yanbo Wang, Takeshi Noda, Hiroshi Segawa, Xudong Yang, Yiqiang Zhang, and Liyuan Han*

Lead-free tin perovskite solar cells (TPSCs) have attracted widespread attention in recent years due to their low toxicity, suitable bandgap, and high carrier mobility. However, the photovoltage and efficiency of TPSCs are still much lower than those of the lead counterparts because of the high trap density and unfavorable band structure in tin perovskite films. To overcome these issues, efficient and stable TPSCs with a graded heterostructure of light-absorbing layer are reported, in which the narrow-bandgap tin perovskite dominates at the bulk, whereas the wide-bandgap tin perovskite is distributed with a gradient from bulk to surface. This heterostructure can selectively extract the photogenerated charge carriers at the perovskite/electron transport layer interface, reduce the density of trap states, and impede the oxidation process of Sn^{2+} to Sn^{4+} in air. As a consequence, this graded heterostructure of tin perovskite layer contributes to an increase of 120 mV in the open-circuit voltage and a maximum power conversion efficiency of 11% for TPSCs with longer operational stability.

1. Introduction

Organic–inorganic metal halide perovskites as ideal materials for the next-generation photovoltaic technique have attracted great attention from all over the world.[1–8] However, the toxicity issue of lead perovskite has been a potential obstacle for the large-scale application. So far, a series of lead-free perovskites based on tin (Sn), germanium (Ge), bismuth (Bi), stibium (Sb), and copper (Cu) have been investigated.[9–13] Among them, tin perovskite materials have been developed as one of the promising candidates for lead-free perovskite absorbers because of their suitable optical bandgap close to the Shockley–Queisser limit and higher charge carrier mobility as compared to their lead-based counterparts.[14–17] However, the performance of tin perovskite solar cells (TPSCs) is still inferior to that of the lead-based counterparts due to the large recombination loss in tin perovskite semiconductors.[18–20]

The oxidation process of Sn^{2+} to Sn^{4+} is thermodynamically favorable, which spontaneously introduces the electronic trap states, acting as the main nonradiative recombination pathway of photogenerated free carriers.[15,21] To suppress the instability of Sn^{2+}, antioxidant additives such as SnF_2, $SnCl_2$, pyrazine, and hydroxybenzene sulfonic acid have been reported as sacrificial agents to prevent the oxidation and improve the carrier lifetime in tin perovskite films.[22–25] Recently, a liquid formic acid was exploited as a volatile reducing solvent for the film deposition to eliminate the Sn^{4+} impurities in SnI_2 precursor.[26] Unsuitable interface band alignment is another factor that induces the voltage loss in TPSCs. The large energy-level offset between tin perovskite and the commonly used electron transport materials suppresses the quasi-Fermi level splitting and provides additional channels that accelerate the trap-assisted recombination process.[27]

Introducing the large-size organic cations such as *n*-butylammonium (BA), phenylethylammonium (PEA), and guanidinium (GA) to form the low-dimensional tin perovskite with a tailored electronic band structure, can efficiently stabilize the Sn^{2+} components and reduce the energy level mismatch in TPSCs.[28–30] For example, Wu and co-workers used the PEA cations to fabricate a 2D–3D bulk heterojunction of tin perovskite film via a bilateral interfacial engineering strategy.[31] This bulk heterojunction significantly reduced the charge recombination rate in TPSCs by the presence of wide-bandgap 2D perovskite phase, resulting in an efficiency of 6.98% and better device stability. In addition, forming a 2D–3D heterojunction has also been applied to other perovskite compositions such as the lead or mixed tin-lead halide perovskites to improve the device performance.[2,32] However, distribution of the low-dimensional

Dr. T. Wu, Dr. D. Cui, Prof. Y. Wang, Prof. X. Yang, Prof. L. Han
State Key Laboratory of Metal Matrix Composites
Shanghai Jiao Tong University
800 Dong Chuan Road, Shanghai 200240, China
E-mail: Han.liyuan@sjtu.edu.cn

Dr. X. Liu, Dr. X. Meng, Dr. T. Noda, Prof. L. Han
Photovoltaic Materials Group, Center for Green Research on Energy and Environmental Materials
National Institute for Materials Science
Tsukuba, Ibaraki 305-0047, Japan

Dr. H. Segawa
Research Center for Advanced Science and Technology
University of Tokyo
Tokyo 153-8904, Japan

Dr. Y. Zhang, Prof. L. Han
School of Materials Science and Engineering
Henan Institute of Advanced Technology
Zhengzhou University
Zhengzhou 450001, China

The ORCID identification number(s) for the author(s) of this article can be found under https://doi.org/10.1002/solr.202000240.

structure in light-absorbing layer is still hard to control, which would impact the carrier transportation and separation by the quantum-well effect, resulting in a compromise of the photovoltaic performance. Therefore, a rational design of the band structure enabling robust carrier transport ability and favorable contact with the electron-selecting materials is required to further increase the efficiency of TPSCs.

In this study, we reported stable and efficient TPSCs with a perovskite graded heterostructure (GHS), in which the narrow-bandgap tin perovskite dominates at the bulk as well as the wide-bandgap tin perovskite distributed with a gradient from bulk to surface to reduce the recombination loss in TPSCs. This perovskite heterostructure was constructed by a sequential cation exchange reaction between the as-prepared formamidinium tin iodide perovskite ($FASnI_3$) and the bulky 4-(trifluoromethyl) benzyl ammonium cations ($TFBA^+$, $CF_3C_6H_5CH_2NH_3^+$). Experimental studies and the theoretical calculation demonstrated that the GHS could selectively extract the photogenerated charge carriers at the perovskite/electron transport layer (C_{60}) interface, reduce the density of trap states in perovskite film, and serve as an energy barrier against the undesirable oxidation of Sn^{2+} components. Attributed to these benefits, we achieved an increase of 120 mV in the open-circuit voltage (V_{oc}) of TPSCs, enabling a maximum power conversion efficiency (PCE) of about 11%. Moreover, the optimized device showed a large improvement in the operational stability, maintaining a PCE more than 10% after 500 h of light soaking (AM 1.5G, 100 mW cm^{-2}) at the maximum power point.

2. Results and Discussion

The $FASnI_3$ perovskite film was prepared using a typical antisolvent method through a one-step deposition process (details can be found in the Experimental Section). To fabricate the GHS of the tin perovskite, the as-prepared $FASnI_3$ film was subsequently dipped in a chloroform solution containing TFBAI salts, followed by thermal annealing to promote the sequential exchange reaction between FA^+ and bulky $TFBA^+$ cations,[33–35] resulting in the formation of wide-bandgap $TFBA_2SnI_4$ perovskite. The exchange process possibly occurring at the surface of the solid-state film due to the large steric effect of bulky $TFBA^+$ cation could hinder the further reaction inside the perovskite crystal, and a structure of $(TFBA_2SnI_4)_x(FASnI_3)_{1-x}$ with graded bandgap alignment is supposed to be constructed, as demonstrated in the following discussion. Here, the GHS was applied in an inverted TPSCs (device structure is shown in **Figure 1**a) to optimize the perovskite/fullerene (C_{60}) interface.

We first conducted X-ray diffraction (XRD) measurement to verify the formation of GHS in perovskite films. As shown in Figure 1b, the XRD pattern of pristine $FASnI_3$ film (marked as control) deposited on the PEDOT:PSS substrate shows diffraction peaks at 14.0°, 24.4°, 28.2°, and 31.7° associated with (100), (102), (200), and (122) crystal planes of the orthorhombic perovskite phase (*Pnma*), respectively.[36] For the perovskite film undergoing a post treatment of TFBAI salts (marked as TFBAI-treated), two additional peaks located at 4.9° and 9.8° were found, assigned to the (100) and (200) crystal planes of the 2D $TFBA_2SnI_4$ perovskite, respectively. To further investigate the

vertical distribution of 2D phase in the film, the grazing incident X-ray diffraction (GIXRD) analysis was performed. Figure S1, Supporting Information, shows the GIXRD patterns of TFBAI-treated perovskite measured at different X-ray incident angles; we can see that the diffraction peak intensity ratio of 3D (100)/2D (100) increases from 5.2 to 13.5 when the X-ray incident angle increases from 0.2° to 1.0°, indicating that the content of $TFBA_2SnI_4$ phase decreases gradually from surface to the inner part of tin perovskite layer.

To study the compositional evolution of perovskite films before and after the TFBAI treatment, we used time-of-flight–secondary ion mass spectrometry (ToF–SIMS) to characterize the depth profile of the corresponding elements (Figure 1c,d). For the control film, the tin (indicated by SnI_2^-) and iodide (indicated by I^-) elements showed a homogeneous distribution from bottom to the top of film. In contrast, the TFBAI-treated sample exhibited an increased concentration of iodide at the top surface, attributed to the formation of iodide-rich $TFBA_2SnI_4$ phase. Furthermore, the concentration of $TFBA^+$ cations (indicated by $CF_3C_6H_5^-$) depicted a gradual decay with increasing probed depth. We also performed the ToF–SIMS 2D mapping analysis to investigate the distribution of $TFBA^+$ cations along the $x–z$ plane of GHS perovskite film (Figure S2, Supporting Information). It was found that the color of $CF_3C_6H_5^-$ signal changes from light yellow (high content) to dark blue (low content) gradually along the z direction, further confirming the formation of GHS. Moreover, X-ray photoelectron spectroscopy (XPS) was used to monitor the variation of binding condition at perovskite surface with the incorporation of $TFBA^+$ cations. Figure 1e shows the high-resolution XPS C 1s spectrums of different perovskite films. For the pristine $FASnI_3$ film, the peaks located at 284.6 and 287.8 eV are assigned to the signals of C—H and C=NH_2^+ bonds on FA^+ cations, respectively. We also found that the intensity of C=NH_2^+ peak clearly decreased in the TFBAI-treated film, whereas two new peaks were detected at 285.9 and 291.4 eV, associated with the C—NH_3^+ bond and the π–π interaction of benzene ring on $TFBA^+$ cations, respectively. In addition, the surface I 3d core levels (I 3d$_{5/2}$ and I 3d$_{3/2}$) of $FASnI_3$ perovskite shift to a higher binding energy after the TFBAI post treatment (Figure S3, Supporting Information), which indicates a variation in the Sn—I bond and further confirms the cation exchange reaction occurred at the tin perovskite surface.[37]

We then studied the impact of TFBAI treatment on the surface morphology of $FASnI_3$ perovskite by the scanning electron microscopy (SEM), as shown in Figure S4, Supporting Information. The top-view SEM images of the $FASnI_3$ film show a polycrystalline structure with many pinholes at grain boundaries, which is consistent with the morphology shown in previous studies.[38,39] After being dipped in 2 mg mL^{-1} TFBAI solution, the perovskite surface was covered with a thin capping layer and the pinholes at grain boundaries almost disappeared. When the concentration of TFBAI solution increased to 5 mg mL^{-1}, aggregation and residues of the unreacted TFBAI salts could be found at the surface with large roughness and poor film morphology, indicating the fact that further reaction between the $FASnI_3$ and $TFBA^+$ cations was prohibited.

To understand the carrier dynamics in different perovskite structures, photoluminescence (PL) characterizations were used in the study. **Figure 2**a shows the steady-state PL spectrums of
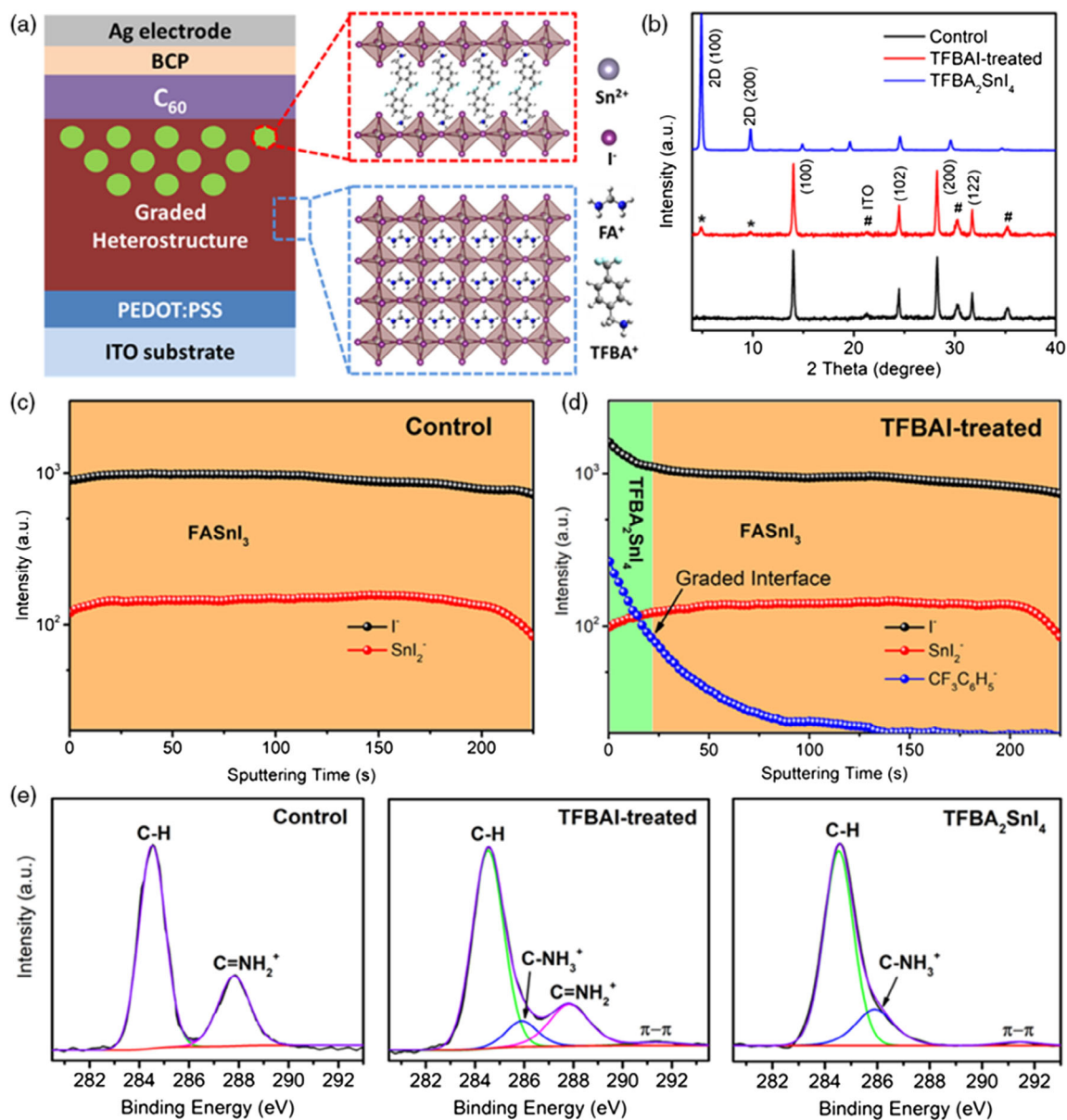
Figure 1. a) Schematic illustration of the device with a structure of ITO/PEDOT:PSS/tin perovskite/C_{60}/BCP/Ag; the inset shows the GHS at the perovskite/fullerene interface. b) XRD patterns of the corresponding perovskite films deposited on the PEDOT:PSS substrate. The diffraction peaks indicated by # and * represent the Bragg reflections of ITO glass and the $TFBA_2SnI_4$ phase in $FASnI_3$ film, respectively. ToF–SIMS depth profiles scanning from the top to the bottom of c) pristine $FASnI_3$ film and d) TFBAI-treated film. e) High-resolution XPS C 1s spectra of the control, TFBAI-treated, and $TFBA_2SnI_4$ films.

pristine $FASnI_3$ and GHS perovskites deposited on the bare glass substrate. The PL peak position of the GHS sample showed a slightly blue shift as compared with that of the control one, which means a decrease in the surface tail states. In addition, the modified perovskite also exhibited a much larger PL quenching of 72% than that of control one (51%) after the introduction of an electron-accepting fullerene layer atop the perovskite films, indicating a high electron-collection efficiency at the GHS/C_{60} interface. Moreover, we measured the time-resolved PL plots fitted with a single exponential mode to extract the carrier lifetime of corresponding perovskite samples (Figure 2b), and the fitting

parameters are shown in Table S1, Supporting Information. PL decay lifetime in the GHS structure was 6.61 ns, about two times higher than that in the $FASnI_3$ perovskites (3.25 ns), associated with a slower trap-assisted carrier recombination rate according to the Shockley–Read–Hall model.[40] In addition, PL lifetime of the GHS perovskite covered with C_{60} significantly decrease to 1.91 ns, shorter than the control/C_{60} sample (2.32 ns), which means that GHS structure can selectively extract the photo-generated electrons under light condition. In addition, space charge limit current (SCLC) method was conducted to estimate the trap density in perovskite films. Figure 2c shows the dark *I–V*
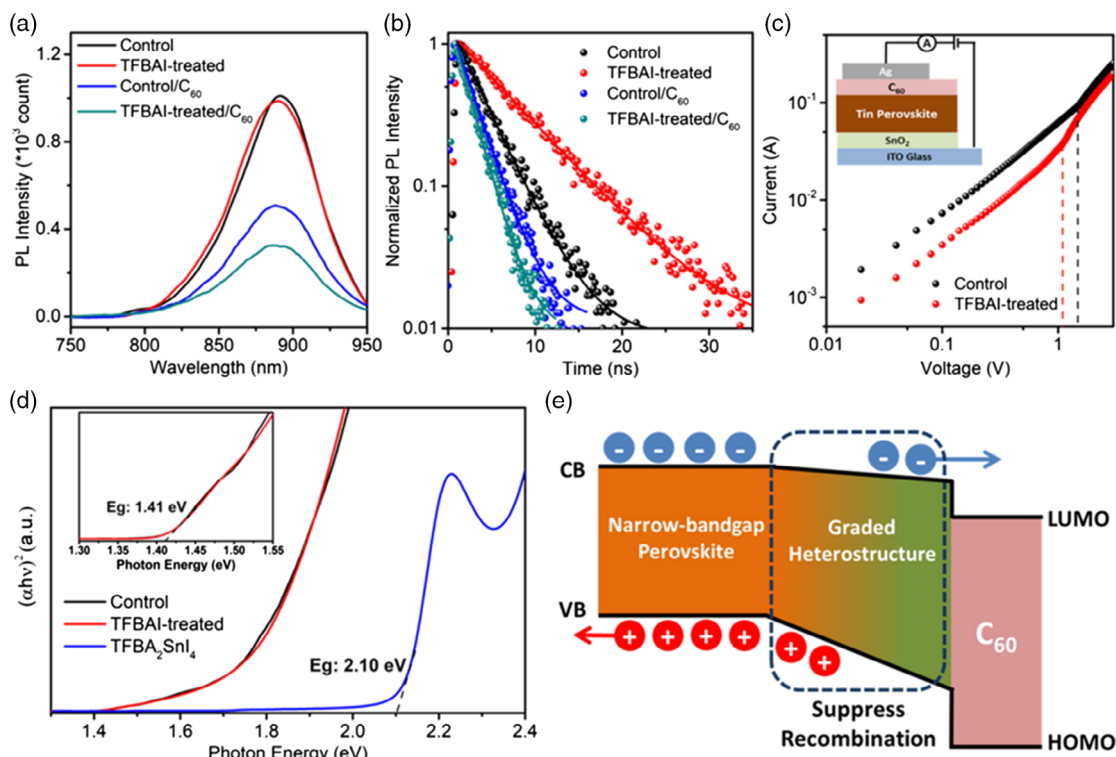
Figure 2. a) Steady-state PL spectrums of the perovskite films without or with an electron-accepting C_{60} capping layer. b) TRPL spectrums of the corresponding samples. c) Dark *I–V* plots of the electron-only device with a structure of ITO/SnO$_2$/tin perovskite/C_{60}/Ag. d) Tauc plots of the perovskite films derived from UV–vis spectrums. e) The schematic band alignment of the GHS at perovskite/C_{60} interface. All the samples for PL measurement were deposited on the bare glass.

curves of the electron-only device with a structure of ITO/SnO$_2$/tin perovskite/C_{60}/Ag; the trap density can be calculated from the onset voltage of trap-filling limit region (V_{TFL}), as shown in Equation (1)

$$N_{trap} = \frac{2\varepsilon_0 \varepsilon_r V_{TFL}}{qd^2}$$ (1)

where ε_0 is the vacuum permittivity, ε_r is the relative dielectric constant (ε_r of the FASnI$_3$ perovskite is estimated at 5.7),[41] q is the unit charge, and d is the thickness of the perovskite film. Based on the V_{TFL} derived from dark *I–V* curves, we can calculate the trap density to be 5.62×10^{16} cm^{-3} and 3.86×10^{16} cm^{-3} for the control and modified perovskite films, respectively, which could be attributed to the passivation effect of large-size organic TFBA$^+$ cations that could effectively reduce the trap states caused by surface vacancy defects.[37,42]

To reveal the mechanism of the enhanced electron-collection efficiency and carrier lifetime, we further studied the band structure of different perovskite samples by measuring the ultraviolet–visible (UV–vis) absorption spectrums (Figure S5a, Supporting Information). The TFBAI-treated sample showed a similar absorption edge around 880 nm as compared with that of the FASnI$_3$ perovskite, corresponding to 1.41 eV of the optical bandgap (Figure 2d), indicating that the UV–vis response of tin perovskite film is not affected by the GHS structure. In contrast, the pure TFBA$_2$SnI$_4$ perovskite showed a narrow UV–vis

response and a wide bandgap of 2.10 eV, about 0.7 eV larger than that of the FASnI$_3$ perovskite. Furthermore, we estimated the shift of surface energy levels using UV photoelectron emission spectrums. As shown in Figure S5b, Supporting Information, the ionization potentials of the electrons ejected from the valence band maximum (VBM) of pristine FASnI$_3$ and TFBA$_2$SnI$_4$ films are −4.95 and −5.66 eV, respectively. Intriguingly, the TFBAI post treatment shifts the surface ionization potential to the value between those of the FASnI$_3$ and TFBA$_2$SnI$_4$ alone (from −5.06 to −5.40 eV with increased concentration of the TFBAI solution, as shown in Figure S5c, Supporting Information), indicating the shift of surface VBM level for tin perovskite is proportional to the amount of incorporated wide-bandgap phase. By subtracting the bandgap of the samples, we can estimate the conduction band minimum (CBM) of FASnI$_3$ and TFBA$_2$SnI$_4$ films to be −3.54 and −3.56 eV, respectively, indicating a type II junction forming in the GHS perovskite (Figure S5d, Supporting Information). On the other side, our ToF–SIMS results indicate that the wide-bandgap phase has a gradient distribution in the vertical direction within the GHS structure. According to the aforementioned discussion, we drew the energy-level alignment at the GHS/C_{60} interface in Figure 2e. The conduction band of the GHS shows a free barrier for electron transport from perovskite to the lowest unoccupied molecular orbital (LUMO) of C_{60}. In contrast, the gradually deeper energy level of the valence band could efficiently block the holes generating from

narrow-bandgap FASnI$_3$ phase, leading to a reduced charge recombination rate at the electron transport layer interface.[43]

Apart from the modification of interfacial band alignment, we confirmed that TFBA$^+$ cations in wide-bandgap phase with large steric hindrance could also serve as an energy barrier to suppress the permeation of oxygen molecules into the perovskite lattice by the density functional theory (DFT) calculation. **Figure 3**a,b showed the oxygen-absorbed models of FASnI$_3$ and TFBA$_2$SnI$_4$ perovskites along the (100) slabs, and both two models underwent a structure-relaxation process before the simulation. The oxygen molecule was first put on an octahedral interstice of the corner-sharing [SnI$_6$]$^{4-}$ units (Figure S6, Supporting Information) and then moved close to the perovskite lattice gradually, as highlighted by the sequence numbers. During this process, we calculated the formation energy of perovskite–oxygen composites at different positions and then summarized the corresponding values in Figure 3c. For the FASnI$_3$ model, the formation energy decreases from −0.21 to −0.7 eV when the oxygen molecule moves close to the perovskite lattice, indicating that the oxygen permeation is thermodynamically favorable, which is related to the stable N—H...O hydrogen bonding interactions between the FA$^+$ cations and oxygen molecules, as proved in our previous work.[44] In the case of TFBA$_2$SnI$_4$ model, the formation energy shows a slight increase from −0.23 to 0.14 eV with a reduced distance between

oxygen molecule and the Sn–I–Sn frameworks, which could be attributed to the large steric effect of 4-(trifluoromethyl)phenyl unit that provides additional energy barrier against the oxygen absorption.

To confirm our speculation, we put the perovskite films in air and monitored the variation of surface Sn 3d core level via XPS analysis. As shown in Figure 3d,e, the Sn 3d$_{5/2}$ signal could be separated into two individual peaks at 486.4 and 487.2 eV, associated with the Sn^{2+} and Sn^{4+} components, respectively. After being exposed in air for 4 h, the atomic ratio of Sn^{4+} in control films increases to 76.92%, much higher than the value of fresh sample (22.65%). Interestingly, no clear change in the Sn^{4+} ratio was found in the TFBAI-treated films, demonstrating a better environmental stability of the tin perovskite with GHS structure. We also measured the UV–vis absorption spectra of the perovskite films with different air-exposed time to interpret the possible degradation process. As shown in Figure S7, Supporting Information, the control film exhibited an absorption loss of 34% at 600 nm after 4 h aging, indicating a large amount of nonperovskite phase induced by the Sn^{2+} oxidation. In contrast, the TFBAI-treated film could keep over 90% of the initial light response during the aging process.

Subsequently, we studied the device performance of TPSCs (ITO/PEDOT:PSS/tin perovskite/C$_{60}$/BCP/Ag) assembled with different perovskite structures, and the cross-section SEM image
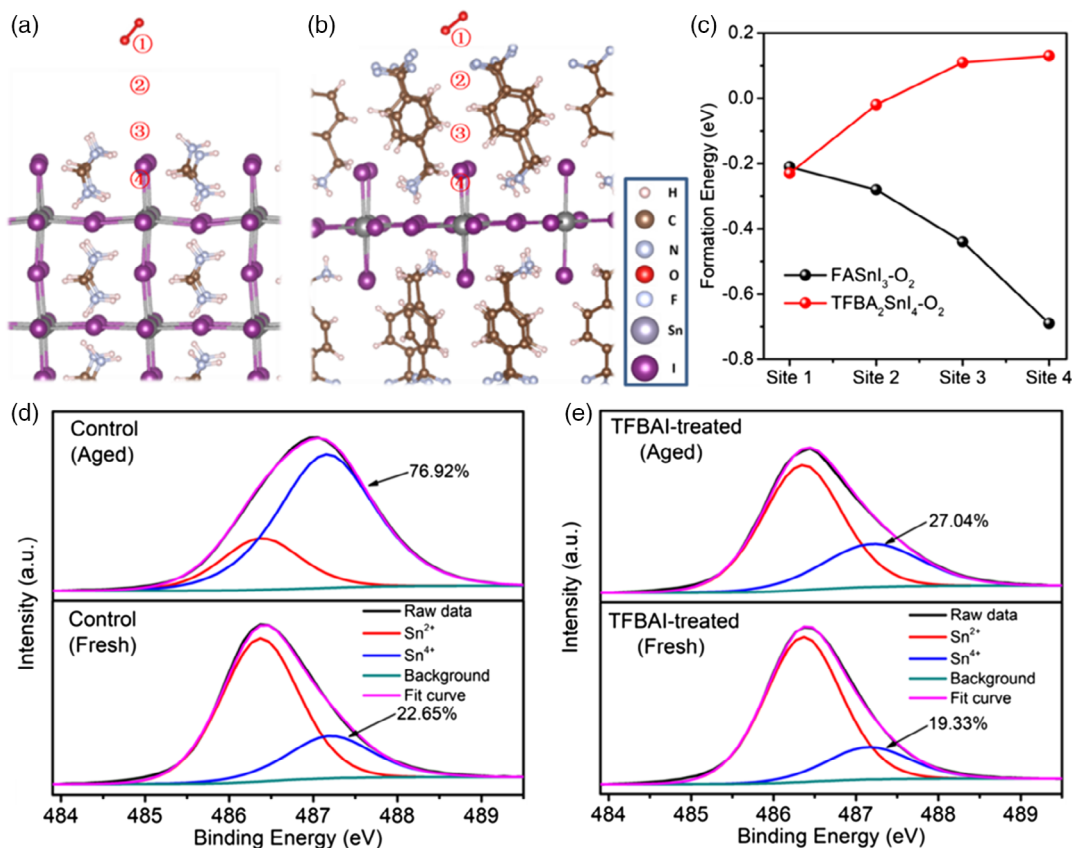

Figure 3. The relaxed structures of the oxygen-absorbed a) FASnI$_3$ and b) TFBA$_2$SnI$_4$ models along the (100) slabs for DFT calculation. c) Calculated formation energy of the perovskite models with oxygen molecule at different sites. High-resolution XPS Sn 3d spectrums of the d) FASnI$_3$ and e) TFBAI-treated FASnI$_3$ films before and after aged in air for 4 h.
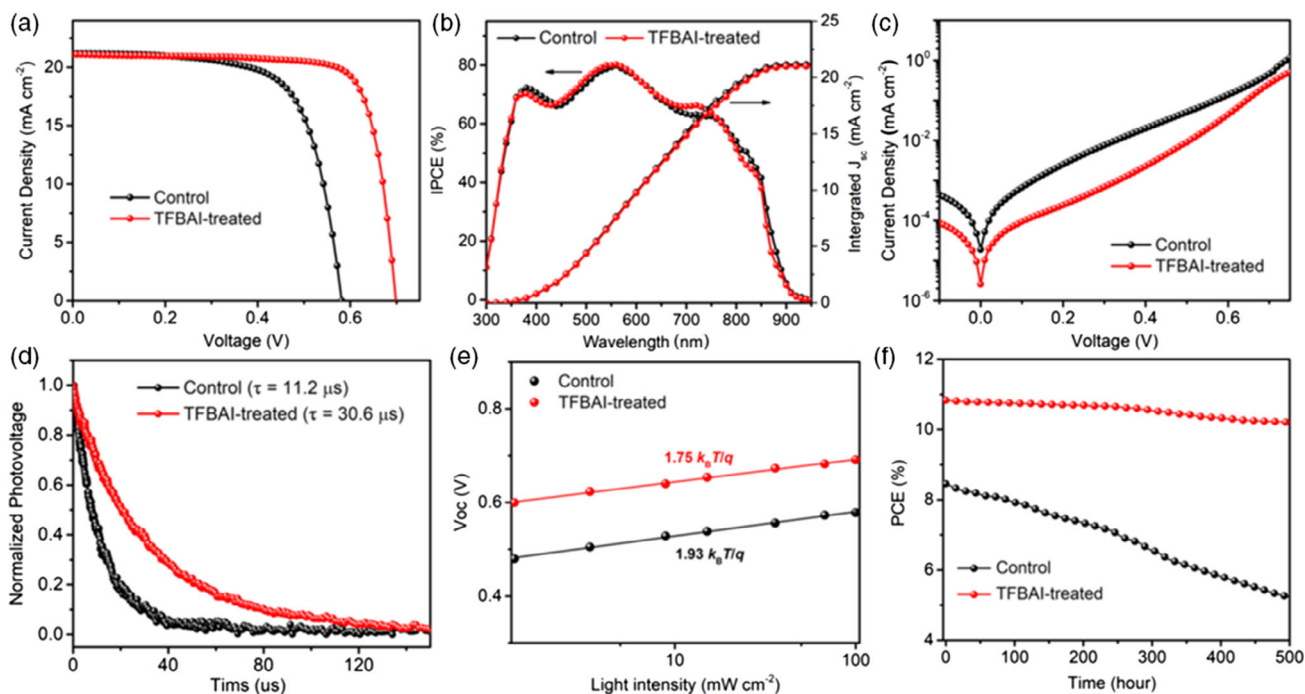
Figure 4. a) J–V curves of the best-performing devices assembled with control and TFBAI-treated perovskites measured under reverse scan; the active area is 0.09 cm². b) IPCE of the devices. c) Dark current plots of the devices. d) TPV measurement for the TPSCs. e) V_{OC} versus illumination intensity for the devices. f) PCE decay plots of the TPSCs measured under the maximum power point in air; the applied biases corresponding to the maximum power point are 0.42 and 0.60 V for the control and TFBAI-treated devices, respectively, and the operating temperature is fixed at 25 °C. All the cells that went through the aging test were encapsulated.

of the optimized device was shown in Figure S8, Supporting Information. **Figure 4**a shows the current density–voltage (J–V) curves of the champion FASnI₃-based cells without or with TFBAI treatment. The control device displayed an V_{oc} of 0.58 V, a short-circuit current density (J_{sc}) of 21.29 mA cm⁻², a fill factor (FF) of 69.1%, and a PCE of 8.53% at the reverse scan. Meanwhile, the device treated with 2 mg mL⁻¹ TFBAI showed a much higher V_{oc} of 0.70 V, a J_{sc} of 21.07 mA cm⁻², an FF of 74.3%, and a PCE of 10.96% with very stable power output (Figure S9, Supporting Information). The large improvement in the device V_{oc} could be attributed to the following reasons. 1) The graded band structure of GHS perovskite is better for the charge separation and extraction at the perovskite/charge transport layer interface, as compared to the pristine narrow-bandgap FASnI₃ perovskite with large energy-level offset at the heterojunction. 2) The passivation effect of TFBA ammonium molecules significantly reduced the trap density in perovskite films, as confirmed by the SCLC measurement, resulting in less trap-assisted recombination in TPSCs.[45] 3) The GHS perovskite film showed a pinhole-free morphology compared with the pristine FASnI₃ film, which can also reduce the charge recombination rate and improve the photovoltage in TPSCs. In addition, the modified devices showed a higher reproducibility with a standard deviation of 0.65% for the PCE as compared with that of the control devices (1.12%) based on the statistics of 40 cells (Figure S10, Supporting Information). Furthermore, the J–V hysteresis of solar cells becomes smaller after the TFBAI treatment (Figure S11, Supporting Information), which could be attributed to the reduced recombination channels and lower trap

density in the GHS structure. We also found that higher concentration (3 mg mL⁻¹) of the TFBAI treatment would lead to a decrease in FF and a larger J–V hysteresis in the TPSCs, which is attributed to the fact that excess TFBAI salts serving as an insulating agent on perovskite surface could hinder the electron extraction process and cause the energy-level mismatch at the tin perovskite/C₆₀ interface.[46] In addition, incident photon-to-electron conversion efficiency (IPCE) spectrums were used to characterize the photo-response of corresponding solar cells (Figure 4b). The integrated J_{sc} of control and TFBAI-treated devices were calculated to be 21.14 and 20.99 mA cm⁻², respectively, consistent with those obtained by the J–V curves within a standard error less than 1%.

To further reveal the recombination dynamics in a completed device, we measured the dark current plots of the TPSCs, as shown in Figure 4c. The device with TFBAI treatment exhibited a relatively lower saturation current density ($J_0 = 4.1 \times 10^{-5}$ mA cm⁻²) than that of the control one ($J_0 = 2.8 \times 10^{-4}$ mA cm⁻²), associated with less charge recombination in the solar cells. Moreover, transient photovoltage (TPV) analysis was conducted to derive the charge recombination lifetime in the TPSCs (Figure 4d). The TFBAI-treated device showed a substantially slower decay of the TPV than that of the pristine one, suggesting that charge recombination pathways in completed device are efficiently blocked by the GHS structure. We then tested V_{oc} versus illumination intensity curves to identify the voltage loss caused by the interface carrier recombination (Figure 4e). The ideal factor (n) of TFBAI-treated device calculated from the slop (nk_BT/q) is 1.75, smaller than

that of the control cell (1.93), associated with a less voltage loss in the solar cells, as shown in the Equation (2), where E_g is the bandgap of perovskite absorber, k_B is the Boltzmann constant, I is the light intensity, T is the temperature, and I_0 is a constant with the same unit as I.

$$qV_{oc} = E_g - nk_B T \ln\left(\frac{I_0}{I}\right) \qquad (2)$$

In addition, we measured the evolution of PCE versus the time for the control and TFBAI-treated solar cells (with encapsulation) under continuous light soaking (AM 1.5G, 100 mW cm^{-2}) at the maximum power point in air (Figure 4f). The device with TFBAI treatment still kept the efficiency over 10% with negligible PCE decay after 500 h of operation, whereas the control one showed a 35% loss of its initial efficiency after the aging process. In addition, the J–V curves and device parameters versus the operational time are summarized in Figure S12 and Table S2, Supporting Information. We found that the PCE loss of TFBAI-treated device is mainly caused by the decrease in FF, which occurred after 300 h of the operation. Possible reason is that the long-term operation causes a degradation of the metal electrode and thus increases the series resistance of solar cells.[47] In contrast, we extracted the 80% lifetime (T80) of TPSCs from the PCE decay curves; the T80 values were estimated to be 282 and 1643 h for the control and TFBAI-treated devices, respectively, indicating a significant improvement in the device working lifetime by introducing the GHS structure. Furthermore, the operational stability of TPSCs under moisture and heat conditions was measured for discussion. As shown in Figure S13, Supporting Information, the pristine FASnI$_3$ device shows a large PCE decay of about 22% after 100 h of operation at 60 °C with a relative humidity of 60%. In contrast, the TFBAI-treated device presents an efficiency loss less than 5% after the aging test. Possible reason is that the layered TFBA$_2$SnI$_4$ phase could suppress the decomposition of perovskite crystal induced by heat or moisture due to its high formation energy.[29] We also tested the stability of unencapsulated devices to demonstrate the potential benefits of GHS. As shown in Figure S14, Supporting Information, the control device completely degraded after exposed in air for 40 h, but the TFBAI-treated device could maintain 78% of the original PCE after 100 h of storage in air.

3. Conclusions

In summary, we first proposed a strategy for highly efficient TPSCs based on constructing a GHS of tin halide perovskite to optimize the perovskite/electron transport layer interface. Our results and discussions confirmed that the GHS with gradually increased bandgap and deeper energy level of the valence band from bulk to the interface, could selectively extract the photogenerated electron, decrease the trap density in perovskite film, and increase the energy barrier against the oxidation of Sn^{2+} in air. Consequently, the solar cells with GHS structure obtained a high efficiency about 11% for the fresh device and still kept a PCE over 10% after 500 h of operation at the maximum power point. More importantly, this work also provides a new route to improve the photovoltage of TPSCs via precisely controlling the phase distribution and band structure of tin perovskite absorbers, and can be further applied to improve the efficiency of other tin-based or mixed tin–lead perovskite solar cells.

4. Experimental Section

Device Fabrication: The patterned ITO glass substrates were cleaned via sequential ultrasonication in detergent, deionized water, acetone, and isopropanol for 15 min, respectively. Then the substrates were treated with UV ozone for 30 min. The (PEG)-PEDOT: PSS solution was spin-coated onto the ITO substrate at 4000 rpm for 30 s and then annealed at 150 °C for 15 min.[46] After that, the substrates were immediately transferred into the glovebox. For the deposition of tin perovskite film, the precursor solution composed of 0.9 M SnI$_2$, 0.9 M FAI, and 0.09 M SnF$_2$ in dimethyl sulfoxide (DMSO) was stirred for 2 h at room temperature. Then, the solution was spin-coated onto the (PEG)-PEDOT: PSS layer at 1000 rpm for 12 s and at 5000 rpm for 48 s; 140 μL chlorobenzene was dripped onto the perovskite film after 30 s of the second process. After the one-step deposition process, the as-prepared FASnI$_3$ film without thermal annealing was dipped in a chloroform solution with different concentration of the TFBAI salt (from 1 to 5 mg mL^{-1}) for 10 s to construct the GHS structure, followed by the spin-coating process at 5000 rpm for 30 s to remove the organic solvent. All the control and TFBAI-treated films were annealed at 65 °C for 10 s and then at 100 °C for 20 min to promote the growth of perovskite crystal. For the preparation of TFBA$_2$SnI$_4$ film, precursor solution composed of 0.6 M SnI$_2$, 1.2 M TFBAI, and 0.06 M SnF$_2$ in DMSO was spin-coated onto the substrate at 1000 rpm for 10 s and at 4000 rpm for 30 s, and annealed at 100 °C for 10 min. Then, 40 nm fullerene C$_{60}$, 8 nm BCP, and 70 nm Ag electrode were sequentially evaporated on the perovskite layer under vacuum level of 10^{-4} Pa. The active area of the device was defined as 0.09 cm^2 with a black metal mask.

Film Characterization: The morphology of the films and devices were observed by the SEM images, measured on the Hitachi SU8000 field-emission SEM. The XRD was measured by SmartLab 9 kW X-ray diffractometer using Cu Kα radiation (λ = 1.54050 Å). The UV–vis spectra were measured by a Shimadzu UV-vis 3600 spectrophotometer. The XPS spectra were carried out by PHI Quantera SXM (ULVAC-PHI) with X-ray source of Al Kα (mono). The steady-state PL and TRPL were measured by a Hamamatsu C12132 fluorescence lifetime spectrometer with an excitation wavelength of 450 nm. UV photoelectron emission spectra were measured by Riken-Keiki AC-3 instrument. The TPV curves were measured by a platform for all-in-one characterization of solar cells and organic light emitting diodes (PAIOS) of FLUXim Company at open circuit condition; the pulse length of a white light is 1 ms, background light of 0.09 Sun (9 mW cm^{-2}) was applied. ToF–SIMS measurements were performed using the focused ion beam ToF–SIMS spectrometer (GAIA3 GMU Model 2016, Czech). A 30 keV Bi$^+$ ion beam was used as the primary ion beam to peel the samples with an analysis area of 10 × 10 μm^2. The SCLC plots and dark J–V curves were measured by a multifunctional electrochemical analysis instrument (Zahner, Germany) using a linear voltage sweep mode with a constant step voltage of 20 mV.

Device Characterization: The J–V curves were measured by a solar simulator with standard air mass AM 1.5 sunlight (100 mW cm^{-2}, WXS-155S-10, Wacom Denso) under forward scan (−0.1 to 0.7 V) or reverse scan (0.7 to −0.1 V) by a fixed step voltage of 10 mV and delay time of 50 ms.[48] The reference cell used for the spectral correction was calibrated by the measurement team at Research Center for Photovoltaics in the National Institute of Advanced Industrial Science and Technology (AIST), Japan. Monochromatic IPCE spectra were measured by a monochromatic incident light of 1 × 10^{16} photons cm^{-2} in director current mode (CEP-2000BX, Bunko–Keiki). The light intensity of the solar simulator was calibrated by a standard silicon solar cell. The operation stability of control and TFBAI treated cells was tested on a solar-cell light-resistance test system (Model BIR-50, Bunko–Keiki) with a Class AAA solar simulator. All the cells were first encapsulated according to our previous reports for operation stability test.[43]

Supporting Information

Acknowledgements

Conflict of Interest

The authors declare no conflict of interest.

Keywords

[1] M. Kim, G. H. Kim, T. K. Lee, I. W. Choi, H. W. Choi, Y. Jo, Y. J. Yoon, J. W. Kim, J. Lee, D. Huh, H. Lee, S. K. Kwak, J. Y. Kim, D. S. Kim, *Joule* **2019**, *3*, 2179.

[2] E. H. Jung, N. J. Jeon, E. Y. Park, C. S. Moon, T. J. Shin, T. Y. Yang, J. H. Noh, J. Seo, *Nature* **2019**, *567*, 511.

[3] P. Cui, D. Wei, J. Ji, H. Huang, E. Jia, S. Dou, T. Wang, W. Wang, M. Li, *Nat. Energy* **2019**, *4*, 150.

[4] N. J. Jeon, H. Na, E. H. Jung, T. Y. Yang, Y. G. Lee, G. Kim, H. W. Shin, S. Il Seok, J. Lee, J. Seo, *Nat. Energy* **2018**, *3*, 682.

[5] W. Chen, Y. Wu, Y. Yue, J. Liu, W. Zhang, X. Yang, H. Chen, E. Bi, I. Ashraful, M. Gratzel, L. Han, *Science* **2015**, *350*, 944.

[6] Q. Jiang, Y. Zhao, X. Zhang, X. Yang, Y. Chen, Z. Chu, Q. Ye, X. Li, Z. Yin, J. You, *Nat. Photonics* **2019**, *13*, 460-466.

[7] Y. Wang, T. Wu, J. Barbaud, W. Kong, D. Cui, H. Chen, X. Yang, L. Han, *Science* **2019**, *365*, 687-691.

[8] T. Wu, Y. Wang, X. Li, Y. Wu, X. Meng, D. Cui, X. Yang, L. Han, *Adv. Energy Mater.* **2019**, *9*, 1803766.

[9] T. B. Song, T. Yokoyama, S. Aramaki, M. G. Kanatzidis, *ACS Energy Lett.* **2017**, *2*, 897.

[10] B. Saparov, F. Hong, J. P. Sun, H. S. Duan, W. Meng, S. Cameron, I. G. Hill, Y. Yan, D. B. Mitzi, *Chem. Mater.* **2015**, *27*, 5622.

[11] D. Cortecchia, H. A. Dewi, J. Yin, A. Bruno, S. Chen, T. Baikie, P. P. Boix, M. Grätzel, S. Mhaisalkar, C. Soci, N. Mathews, *Inorg. Chem.* **2016**, *55*, 1044.

[12] T. Krishnamoorthy, H. Ding, C. Yan, W. L. Leong, T. Baikie, Z. Zhang, M. Sherburne, S. Li, M. Asta, N. Mathews, S. G. Mhaisalkar, *J. Mater. Chem. A* **2015**, *3*, 23829.

[13] S. Öz, J. C. Hebig, E. Jung, T. Singh, A. Lepcha, S. Olthof, F. Jan, Y. Gao, R. German, P. H. M. van Loosdrecht, K. Meerholz, T. Kirchartz, S. Mathur, *Sol. Energy Mater. Sol. C.* **2016**, *158*, 195.

[14] F. Hao, C. C. Stoumpos, D. H. Cao, R. P. H. Chang, M. G. Kanatzidis, *Nat. Photonics* **2014**, *8*, 489.

[15] M. H. Kumar, S. Dharani, W. L. Leong, P. P. Boix, R. R. Prabhakar, T. Baikie, C. Shi, H. Ding, R. Ramesh, M. Asta, M. Graetzel, S. G. Mhaisalkar, N. Mathews, *Adv. Mater.* **2014**, *26*, 7122.

[16] N. K. Noel, S. D. Stranks, A. Abate, C. Wehrenfennig, S. Guarnera, A. A. Haghighirad, A. Sadhanala, G. E. Eperon, S. K. Pathak, M. B. Johnston, A. Petrozza, L. M. Herz, H. J. Snaith, *Energy Environ. Sci.* **2014**, *7*, 3061.

[17] S. J. Lee, S. S. Shin, J. Im, T. K. Ahn, J. H. Noh, N. J. Jeon, S. I. Seok, J. Seo, *ACS Energy Lett.* **2018**, *3*, 46.

[18] F. Hao, C. C. Stoumpos, P. Guo, N. Zhou, T. J. Marks, R. P. H. Chang, M. G. Kanatzidis, *J. Am. Chem. Soc.* **2015**, *137*, 11445.

[19] T. M. Koh, T. Krishnamoorthy, N. Yantara, C. Shi, W. L. Leong, P. P. Boix, A. C. Grimsdale, S. G. Mhaisalkar, N. Mathews, *J. Mater. Chem. A* **2015**, *3*, 14996.

[20] S. J. Lee, S. S. Shin, Y. C. Kim, D. Kim, T. K. Ahn, J. H. Noh, J. Seo, S. I. Seok, *J. Am. Chem. Soc.* **2016**, *138*, 3974.

[21] K. P. Marshall, M. Walker, R. I. Walton, R. A. Hatton, *Nat. Energy* **2016**, *1*, 16178.

[22] W. Liao, D. Zhao, Y. Yu, C. R. Grice, C. Wang, A. J. Cimaroli, P. Schulz, W. Meng, K. Zhu, R. G. Xiong, Y. Yan, *Adv. Mater.* **2016**, *28*, 9333.

[23] C. M. Tsai, N. Mohanta, C. Y. Wang, Y. P. Lin, Y. W. Yang, C. L. Wang, C. H. Hung, E. W. G. Diau, *Angew. Chem., Int. Edit.* **2017**, *129*, 14007.

[24] T. B. Song, T. Yokoyama, C. C. Stoumpos, J. Logsdon, D. H. Cao, M. R. Wasielewski, S. Aramaki, M. G. Kanatzidis, *J. Am. Chem. Soc.* **2017**, *139*, 836.

[25] Q. Tai, X. Guo, G. Tang, P. You, T. W. Ng, D. Shen, J. Cao, C. K. Liu, N. Wang, Y. Zhu, C. S. Lee, F. Yan, *Angew. Chem., Int. Edit.* **2019**, *58*, 806.

[26] X. Meng, T. Wu, X. Liu, X. He, T. Noda, Y. Wang, H. Segawa, L. Han, *J. Phys. Chem. Lett.* **2020**, *11*, 2965.

[27] X. Jiang, F. Wang, Q. Wei, H. Li, Y. Shang, W. Zhou, C. Wang, P. Cheng, Q. Chen, L. Chen, Z. Ning, *Nat. Commun.* **2020**, *11*, 1245.

[28] D. H. Cao, C. C. Stoumpos, T. Yokoyama, J. L. Logsdon, T. B. Song, O. K. Farha, M. R. Wasielewski, J. T. Hupp, M. G. Kanatzidis, *ACS Energy Lett.* **2017**, *2*, 982.

[29] Y. Liao, H. Liu, W. Zhou, D. Yang, Y. Shang, Z. Shi, B. Li, X. Jiang, L. Zhang, L. N. Quan, R. Q. Bermudez, B. R. Sutherland, Q. Mi, E. H. Sargent, Z. Ning, *J. Am. Chem. Soc.* **2017**, *139*, 6693.

[30] F. Wang, X. Jiang, H. Chen, Y. Shang, H. Liu, J. Wei, W. Zhou, H. He, W. Liu, Z. Ning, *Joule* **2018**, *2*, 2732.

[31] C. Ran, J. Xi, W. Gao, F. Yuan, T. Lei, B. Jiao, X. Hou, Z. Wu, *ACS Energy Lett.* **2018**, *3*, 713.

[32] D. Ramirez, K. Schutt, Z. Wang, A. J. Pearson, E. Ruggeri, H. J. Snaith, S. D. Stranks, F. Jaramillo, *ACS Energy Lett.* **2018**, *3*, 2246.

[33] Y. Bai, S. Xiao, C. Hu, T. Zhang, X. Meng, H. Lin, Y. Yang, S. Yang, *Adv. Energy Mater.* **2017**, *7*, 1701038.

[34] D. S. Lee, J. S. Yun, J. Kim, A. M. Soufiani, S. Chen, Y. Cho, X. Deng, J. Seidel, S. Lim, S. Huang, A. W. Y. Ho-Baillie, *ACS Energy Lett.* **2018**, *3*, 647.

[35] Y. Cho, A. M. Soufiani, J. S. Yun, J. Kim, D. S. Lee, J. Seidel, X. Deng, M. A. Green, S. Huang, A. W. Y. Ho-Baillie, *Adv. Energy Mater.* **2018**, *8*, 1703392.

[36] T. Wu, X. Liu, X. He, Y. Wang, X. Meng, T. Noda, X. Yang, L. Han, *Sci. China Chem.* **2020**, *63*, 107.

[37] Y. Wang, T. Zhang, M. Kan, Y. Li, T. Wang, Y. Zhao, *Joule* **2018**, *2*, 2065–2075.

[38] E. Jokar, C. H. Chien, A. Fathi, M. Rameez, Y. H. Chang, E. W. G. Diau, *Energy Environ. Sci.* **2018**, *11*, 2353.

[39] X. Meng, J. Lin, X. Liu, X. He, Y. Wang, T. Noda, T. Wu, X. Yang, L. Han, *Adv. Mater.* **2019**, *31*, 1903721.

[40] W. Tress, M. Yavari, K. Domanski, P. Yadav, B. Niesen, J. P. Correa Baena, A. Hagfeldt, M. Graetzel, *Energy Environ. Sci.* **2018**, *11*, 151.

[41] C. Ran, W. Gao, J. Li, J. Xi, L. Li, J. Dai, Y. Yang, X. Gao, H. Dong, B. Jiao, I. Spanopoulos, C. D. Malliakas, X. Hou, M. G. Kanatzidis, Z. Wu, *Joule* **2019**, *3*, 3072.

[42] X. Zheng, B. Chen, J. Dai, Y. Fang, Y. Bai, Y. Lin, H. Wei, Xiao C. Zeng, J. Huang, *Nat. Energy* **2017**, *2*, 17102.

[43] Y. Wu, X. Yang, W. Chen, Y. Yue, M. Cai, F. Xie, E. Bi, A. Islam, L. Han, *Nat. Energy* **2016**, *1*, 16148.

[44] X. He, T. Wu, X. Liu, Y. Wang, X. Meng, J. Wu, T. Noda, X. Yang, Y. Moritomo, H. Segawa, L. Han, *J. Mater. Chem. A* **2020**, *8*, 2760.

[45] T. Wu, Y. Wang, Z. Dai, D. Cui, T. Wang, X. Meng, E. Bi, X. Yang, L. Han, *Adv. Mater.* **2019**, *31*, 1900605.

[46] X. Liu, Y. Wang, F. Xie, X. Yang, L. Han, *ACS Energy Lett.* **2018**, *3*, 1116.

[47] E. Bi, W. Tang, H. Chen, Y. Wang, J. Barbaud, T. Wu, W. Kong, P. Tu, H. Zhu, X. Zeng, J. He, S. I. Kan, X. Yang, M. Grätzel, L. Han, *Joule* **2019**, *3*, 2748.

[48] M. Yin, F. Xie, X. Li, Y. Wu, X. Yang, F. Ye, Y. Wang, J. He, W. Tang, E. Bi, H. Chen, L. Han, *Appl. Phys. Express* **2017**, *10*, 076601.